

Simulation and Modeling of the *Rhodobacter sphaeroides* Bacterial Reaction Center II: Primary Charge Separation

Matteo Ceccarelli[†]

CECAM, Centre Européen de Calcul Atomique et Moléculaire, Ecole Normale Supérieure de Lyon,
46 Allée d'Italie, 69364 Lyon, France

Massimo Marchi*

Commissariat à l'Energie Atomique, DSV-DBJC-SBFM, Centre d'Études, Saclay,
91191 Gif-sur-Yvette Cedex, France

Received: March 20, 2003

This paper is focused on the molecular dynamics modeling of the primary charge separation in the photosynthetic reaction center (RC) of *Rhodobacter sphaeroides*. The kinetic parameters for the electron transfer along the active (L) and inactive (M) sides were obtained from a long MD trajectory, 3.4 ns, of the RC in an amphiphilic environment made of detergent and water. Both nuclear and electronic polarizations are explicitly included in our calculation. With no postprocessing parameter fit, our modeling computes, for two different charge distributions, the driving forces for the transfer of an excess electron to B_L and H_L from P*, in good agreement with experiments. The multiexponential kinetics of the primary charge separation is also predicted, consistent with experimentally observed kinetics. The decay of the P* state is composed of four characteristic times due to both the conformational heterogeneity of the protein and the two possible mechanisms, superexchange and sequential. At room temperature, the latter is favored over superexchange with decay rates close to experimental rates. Nevertheless, the proximity between the computed diabatic free-energy surfaces on the L side yields a superexchange electronic coupling matrix element very near its resonance point and, thus, very sensitive to changes in the driving forces. For variations of at most 1.3 kcal mol⁻¹, smaller than the accuracy of our theoretical approach, superexchange might be favored over the two-step mechanism. Finally, our molecular modeling strongly indicates that the position of the diabatic free-energy surfaces for the primary charge separation cannot by itself account for the directionality of the primary charge separation. A strong electrostatic potential around the special pair that favors the polarization of the transferring electron toward regions closer to B_L than to B_M is found. This polarization could significantly increase the electronic coupling between P* and B_L, thus accounting, at least in part, for the directionality of the electron transfer.

I. Introduction

Electron transfer (ET) is one of the most ubiquitous of physical processes. It plays an important role in many fields, ranging from chemistry to biology.¹ In plants, algae and bacteria ETs between simple organic molecules (cofactors) arranged in the interior of protein complexes are a key element of the photosynthetic process. These transfers can be rapid, as fast as a few picoseconds, and highly specific.

In bacteria, reaction center (RC) proteins, simpler in structure and function than those of plants, are located in the cellular membrane and sustain the first steps of photosynthesis. In the mid-1980s, the resolution by X-ray crystallography of the first 3D structures of these membrane proteins for two purple bacteria^{2,3} spurred hopes that a full understanding of the mechanism of bacterial photosynthesis was near. Despite the considerable experimental and theoretical effort, a few aspects of the primary charge separation—the initial step of photosynthesis—are still unexplained.

The RC protein of purple bacteria is composed of three principal subunits called L, M, and H, with the former two in contact with the membrane and the latter in contact with the cytoplasm. The L and M proteins bind in their interior several cofactors arranged with a quasi-symmetric C₂ axis defined from the special pair P, a bacteriochlorophyll dimer, to the non-heme iron, as depicted in Figure 1. In *Rhodobacter (Rb.) sphaeroides*, these cofactors are four bacteriochlorophylls (BChl) and two bacteriopheophytins (BPh) of type *a* and two ubiquinones (UQ₁₀). The primary charge separation occurs after the initial photoexcitation of the special pair to P*, when the excited electron moves to the bacteriopheophytin of the L side (H_L) covering of 17 Å in ~3 ps.

In the wild-type RCs, this electron transfer is highly directional, and no detectable transfer is found along the M side. This directionality is also very robust with respect to mutations. Only in recent times were three point mutations⁴ and β -type mutations, in which the accessory bacteriochlorophyll on the M side is replaced by a bacteriopheophytin^{5,6} or the bacteriopheophytin on the L side is replaced by a bacteriochlorophyll,⁷ shown to be able to produce branching to the M side.

* Corresponding author. E-mail: marchi@villon.saclay cea.fr

[†] Present address: CSCS/ETHZ, Via Cantonale, CH-6928 Manno, Switzerland. E-mail: mcecca@cscs.ch

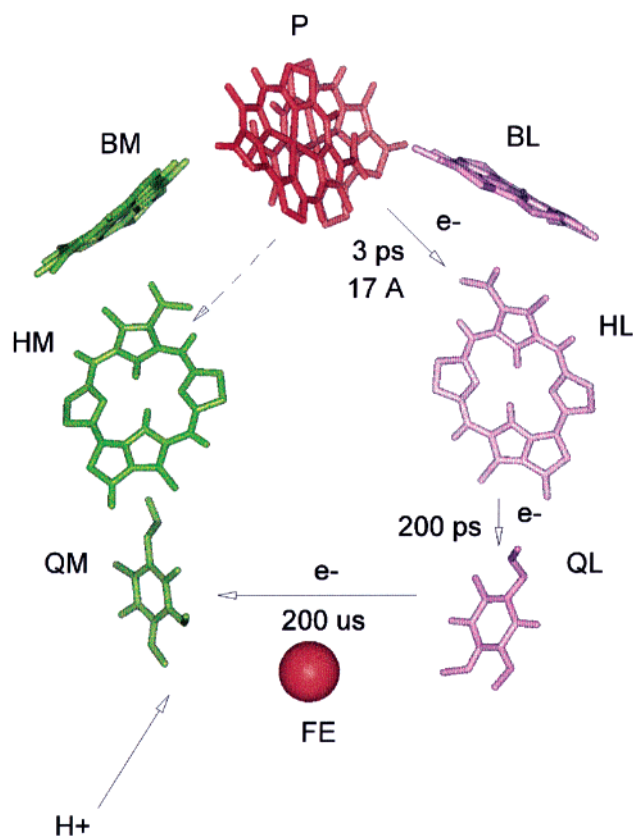


Figure 1. Arrangement of the cofactors in the photosynthetic reaction center of *Rb. sphaeroides*. Arrows show the electron-transfer pathways. P is the special pair composed of two bacteriochlorophylls, B's are the accessory bacteriochlorophylls, H's are bacteriopheophytins, and Q's are the two ubiquinones.

The origin of functional asymmetry is still a matter of debate because the Franck–Condon factor or/and electronic coupling might affect the electron-transfer rate.⁸ In earlier work, the asymmetry of the Franck–Condon term^{9–12} has been invoked as a possible cause of the selective branching. Thus, asymmetric interactions between the protein amino acids and the cofactors of the two sides would determine large activation energies for the M side and forbid ET. In particular, the asymmetry could be either in the accessory bacteriochlorophylls and bacteriopheophytins on the L side, B_L and H_L, or the M side, B_M and H_M.

Electronic coupling between the states has also been investigated. Recently, quantum chemistry techniques have provided the first theoretical estimate of the electronic matrix elements between the cofactors involved in the transfer.^{13,14} These investigations explain the selective branching to the L side with an asymmetry in the electronic coupling between P* and the accessory BChl's. In particular, the properties of the initial electronic state of P* seem to determine the asymmetry. Support for this finding was recently found by experimental investigations.⁴

In the past, two kinetic mechanisms involving one intermediate state have been proposed to explain the high transfer rate of the primary charge separation. For the two-step mechanism, state P⁺B_L[−]H_L with the excess electron localized on B_L is a real intermediate. On the contrary, for superexchange, the P⁺B_L[−]H_L state is only a virtual intermediate that significantly enhances the electronic coupling between the initial, P*, and final states, P⁺B_LH_L[−]. In general, the resolution of time-resolved experi-

ments is not sufficient to demonstrate conclusively the existence of a real intermediate. Nevertheless, in pheophytin-modified RCs, where charge separation to BPh is blocked, P⁺B_L[−]H_L has been isolated, and its driving force has been estimated.^{15,16} Also, recent kinetic experiments on a few mutants of *Rb. sphaeroides*¹⁷ have estimated a small but significant activation energy (~15 meV) by applying the Marcus theory to data at 300 K. This contrasts with experiments¹⁸ showing that the rate constant increases with decreasing temperature. In light of this finding, it is difficult to imagine how a single mechanism of initial electron transfer could work at all temperatures and for all purple bacteria RCs.¹⁹

In recent time-resolved experiments, the multiexponential nature of primary charge separation in wild-type and mutated RCs has been analyzed. (See ref 20 and references therein.) Although mechanisms involving the thermal repopulation of the P* state from P⁺B_LH_L[−],²¹ so-called parking states in the inactive branch,²² and two or more conformational states for the excess electron have been advocated, the origin of multiexponential behavior is not yet clear. For the wild-type RCs of *Rb. sphaeroides* and *Rb. capsulatus*, a shorter time scale around 3 ps and a longer one around 10 ps have been observed.

In this paper, we report on a theoretical investigation of the primary charge separation in *Rb. sphaeroides*. Our main focus has been to study the kinetics mechanism and the functional asymmetry of this electron transfer by molecular modeling and molecular dynamics (MD) simulations. Electron-transfer rates can be estimated through the calculation of the kinetic parameters of a linearly responding spin-boson model corresponding to the excess electron states of the RC interacting with their milieu. (See for instance refs 8 and 23.) To study electron transfer along each branch of the RC, we used the three-state reduced model for electron transfer developed in ref 9 by Chandler and co-workers.

Others have simulated electron transfer in RC proteins. To our knowledge, the very first MD simulation of a RC protein was performed on the RC of *Blastochloris* (Bl.), formerly called *Rhodospseudomonas viridis*,^{24,25} and used geometric constraints (i.e., only atoms in a region near the chromophores were allowed to move) to limit the computational resources needed for the simulation. Similar MD approaches were used by others⁹ in longer simulations. Effects due to the environment surrounding the RC (membrane and solvent) were first accounted for by Warshel, Parson, and co-workers by using effective models for the dielectric response. (Reference 26 provides a comprehensive bibliography from this group.) More recently, MD simulations concerned with the dynamics of the P* state were carried out for a *Rb. sphaeroides* RC hydrated in explicit water.²⁷

In all previous investigations on electron transfer, knowledge of the primary charge separation driving force was used either to renormalize the kinetic parameters of the spin-boson model⁹ or to tune the heavy approximations on the medium dielectric response.^{10,28} In contrast, by modeling the RC and its environment explicitly, our study for the first time derives reorganization and activation free energies and driving forces directly from first principles without a posteriori renormalization procedures. Moreover, our model includes contributions from electronic and nuclear polarization, which are exact in the limit of our classical linearly responding model.

Indeed, given recent improvements in MD algorithms and the ever increasing power of modern computers, we have been able to simulate atomistically the RC protein of *Rb. sphaeroides* in a realistic model of an amphiphilic environment for a sufficiently long time, 3.4 ns. In our simulation, the transmem-

brane helices of the RC are solvated by a layer of detergent molecules—lauryl dimethyl amino oxide or LDAO, used experimentally to solubilize RC—forming a micellelike environment. This molecular complex is then hydrated by placing it in a MD simulation box filled with explicit water. Because the solubilization of RC proteins in LDAO does not alter their structure and functionality experimentally, our simulated system provides a good model with which to investigate electron and proton transfer in these proteins. Results on the behavior of the detergent complex, its interaction with the protein and the water molecules, and the structural changes affecting the primary charge separation have been reported in a separate paper.²⁹

This paper is organized as follows: In section 2, we give the theoretical foundations for the electron-transfer rate calculation based on a three-state spin-boson model. In section 3, we sketch the MD techniques and the microscopic model used in our simulations. The same section also describes the molecular modeling of the excess electron on each of the RC chromophores and provides details on the electronic polarization model used in the postprocessing of the MD trajectory. In section 4, we report and discuss the results of the calculation of the energy gap on the kinetic parameters and the electrostatic asymmetry of the primary electron transfer. In section 5, we discuss our theoretical results of the kinetics of the primary charge separation with respect to experiment. The paper ends with a summary and conclusion.

II. Theoretical Framework

The Marcus theory of electron transfer^{30–33} is widely used in chemistry and biology to understand and interpret redox reactions. The physical model underlying this theory is the so-called spin-boson model. For the electron transfer between a donor and an acceptor in a dielectric medium such as a liquid or a protein, this corresponds to a two-level system linearly coupled to a harmonic oscillating field or bosonic bath. In the limit of weak electronic coupling between the two states, donor and acceptor, the transition or resonant state is reached by thermal fluctuations when the difference in free energy between the states or the energy gap is close to zero. One of the major results of the Marcus theory is that the energy gap itself is the reaction coordinates for the electron transfer. The resulting free-energy surfaces for electron-transfer reactions along the energy gap coordinate are parabolas with identical curvature. In the framework of the spin-boson model, the energy gap corresponds to the fluctuating field and obeys Gaussian statistics—the corresponding Hamiltonian is harmonic.

The harmonic field of the bath is representative of the dielectric nuclear vibrations and includes only the nuclear modes coupled to the electron transfer. In the specific case of the primary electron transfer, the bath ideally corresponds to the surrounding protein environment. The condition of a harmonic bath is not as restrictive as it might seem: only the degrees of freedom that are relevant to electron transfer need a satisfying linear response (i.e., Gaussian statistics). Thus, the spin-boson model can be and is applied to electron transfer in highly anharmonic environments such as liquids and proteins.⁸

To study the primary charge separation in bacterial RCs, we need to adapt the spin-boson model to handle more than two electronic states. In this study, we use a three-state spin-boson model first developed and applied to RCs by Chandler and co-workers.⁹ In this approach, three states coupled to a harmonic bath (the protein environment) are considered on each of the two branches (M and L): (i) state 1 is the photoexcited $^1P^*BH$

state; (ii) state 2 is the intermediary charge-separated state P^+B^-H ; and (iii) state 3 is the final P^+BH^- state. Such a model has the advantage of not making any assumption about the mechanism for the primary charge separation. There are two possibilities: a two-step and superexchange mechanisms. In the former, state 2 is a real intermediate, and in the latter, it is only a virtual one.

We further imagine that the exchanging electron, represented by a tight-binding wave function (see section 3.2), and the environment interact only via electrostatics. Following ref 9, the diabatic free-energy surfaces for this model depend only on two oscillating fields ($\epsilon_{||}$ and ϵ_{\perp}), which are the reaction coordinates for the electron transfer:

$$\begin{aligned} F_1(\epsilon_{||}, \epsilon_{\perp}) &= \frac{\epsilon_{||}^2}{2\alpha_{||}} + \frac{\epsilon_{\perp}^2}{2\alpha_{\perp}} \\ F_2(\epsilon_{||}, \epsilon_{\perp}) &= F_1(\epsilon_{||}, \epsilon_{\perp}) - b\epsilon_{||} - \epsilon_{\perp} + \Delta\epsilon_{12} \\ F_3(\epsilon_{||}, \epsilon_{\perp}) &= F_1(\epsilon_{||}, \epsilon_{\perp}) - \epsilon_{||} + \Delta\epsilon_{13} \end{aligned} \quad (1)$$

Here, $\alpha_{||}$ and α_{\perp} are defined as the average of the fluctuations of the two reaction coordinates ($\epsilon_{||}$ and ϵ_{\perp}) in state 1 or

$$\begin{aligned} \alpha_{||} &= \beta \langle (\delta\epsilon_{||})^2 \rangle_1 \\ \alpha_{\perp} &= \beta \langle (\delta\epsilon_{\perp})^2 \rangle_1 \end{aligned} \quad (2)$$

$\Delta\epsilon_{ij}$ is the average energy gap, or difference in free energy between two states, and includes a gas-phase contribution, $\Delta G_{ij}^{\text{gas}}$ and a solvation term $\Delta E_{ij}^{\text{solv}}$:

$$\Delta\epsilon_{ij} = \langle \Delta E_{ij} \rangle_1 = \Delta G_{ij}^{\text{gas}} + \langle \Delta E_{ij}^{\text{solv}} \rangle_1 \quad (3)$$

Finally, b is derived by making $\epsilon_{||}$ and ϵ_{\perp} statistically orthogonal or

$$\langle \epsilon_{||}\epsilon_{\perp} \rangle_1 = 0 \quad (4)$$

For a linearly responding system, or a system where $\epsilon_{||}$ and ϵ_{\perp} are Gaussian variables as defined eqs 1, the free-energy surfaces are paraboloids. Thus, $\alpha_{||}$, α_{\perp} , $\Delta\epsilon_{ij}$, and b can be determined readily by calculating the energy gaps during a computer simulation in one of the three states. Indeed, the dynamics of the fluctuating fields ($\epsilon_{||}$ and ϵ_{\perp}) is related to the energy gaps of the three states, and we can write

$$\begin{aligned} \Delta E_{12}(t) &= -b\epsilon_{||}(t) - \epsilon_{\perp}(t) + \Delta\epsilon_{12} \\ \Delta E_{13}(t) &= -\epsilon_{||}(t) + \Delta\epsilon_{13} \\ \Delta E_{23}(t) &= (b-1)\epsilon_{||}(t) + \epsilon_{\perp}(t) + \Delta\epsilon_{23} \end{aligned} \quad (5)$$

The fluctuations of the field and the parameter b are then related to the energy-gap fluctuations of our system by

$$\begin{aligned} \alpha_{13} &\equiv \beta \langle (\delta\Delta E_{13})^2 \rangle_1 = \alpha_{||} \\ \alpha_{12} &\equiv \beta \langle (\delta\Delta E_{12})^2 \rangle_1 = b^2\alpha_{||} + \alpha_{\perp} \\ \alpha_{23} &\equiv \beta \langle (\delta\Delta E_{23})^2 \rangle_1 = (b-1)^2\alpha_{||} + \alpha_{\perp} \end{aligned} \quad (6)$$

From the above identities, we easily obtain the parameters needed to draw the free-energy curves:

$$\alpha_{||} = \alpha_{13} \quad (7)$$

$$\alpha_{\perp} = \frac{\alpha_{12} + \alpha_{23} - \alpha_{13}}{2} \quad (8)$$

$$b = \frac{\alpha_{12} - \alpha_{23} + \alpha_{13}}{2\alpha_{13}} \quad (9)$$

The free energies of our three-state model described by eqs 1 are paraboloids in three dimensions, spanned by the two reaction coordinates representing the two orthogonal directions. Whereas $\epsilon_{||}$ corresponds to the process $1 \rightarrow 3$, $1 \rightarrow 2$ and $2 \rightarrow 3$ are given by linear combination of the two coordinates and depend on the parameter b .

Finally, we write the rate constants for the two-step mechanism

$$k_{12} = \frac{2\pi}{\hbar} \sqrt{\frac{1}{4\pi\lambda_{12}k_B T}} (V_{12})^2 \exp\left[-\frac{G_{12}^*}{k_B T}\right] \quad (10)$$

$$k_{23} = \frac{2\pi}{\hbar} \sqrt{\frac{1}{4\pi\lambda_{23}k_B T}} (V_{23})^2 \exp\left[-\frac{G_{23}^*}{k_B T}\right]$$

and for superexchange

$$k_{13}^s = \frac{2\pi}{\hbar} \sqrt{\frac{1}{4\pi\lambda_{13}k_B T}} (V_{13}^s)^2 \exp\left[-\frac{G_{13}^*}{k_B T}\right] \quad (11)$$

In the above equations, $\lambda_{ij} = (\alpha_{ij}/2)$ is the reorganization energy, and G_{ij}^* , the activation free energy, follows the Marcus theory and is given by

$$G_{ij}^* = \frac{(\lambda_{ij} + \Delta G_{ij}^0)^2}{4\lambda_{ij}} \quad (12)$$

with ΔG_{ij}^0 , the driving force of the reaction, defined as

$$\Delta G_{ij}^0 = F_j^{\min} - F_i^{\min} = \langle \Delta \epsilon_{ij} \rangle_1 - \lambda_{ij} \quad (13)$$

The coupling matrix element for the superexchange mechanism, V_{13}^s , can be written as

$$V_{13}^s = \frac{V_{12}V_{13}}{\Delta G_{12}^0 + \lambda_{12} - b[\Delta G_{13}^0 + \lambda_{13}]} \quad (14)$$

where the expression in the denominator is ΔE_{12} , the energy gap between states 1 and 2, computed at $\Delta E_{13} = 0$.

III. Methods

A. Simulation. The results presented in this paper are based on a 3.4-ns MD simulation of a RC protein of *Rb. sphaeroides* in a water and a detergent solution. The latter component—lauryl dimethyl amino oxide, LDAO, a nonionic amphiphile—is used to protect the transmembrane helices of the RC and provides a micellelike structure to cover the RC hydrophobic regions. All details of the MD simulation are reported elsewhere.²⁹ Briefly, the simulation box contained 1 RC protein enclosed in a micellelike structure of 159 LDAO molecules—9 LDAO molecules were crystallographic—and hydrated by 6323 water molecules for a total of 40 327 atoms. The MD simulations were performed for the neutral system (i.e., with the

electron on the special pair P). The force field for the chromophores and detergent was developed by us and is fully described in ref 34. The AMBER parameter set was used instead for the protein,³⁵ and the TIP3P model was adopted for water.³⁶

The system was first equilibrated at constant pressure and temperature ($P = 0.1$ MPa, $T = 300$ K) for 1 ns, after which a data acquisition run lasting an additional 2.4 ns was performed. In that final stage, the simulation box had a hexagonal-like shape, as shown in Figure 2. The smooth particle mesh Ewald technique (SPME)³⁷ was used to handle electrostatic interaction in combination with a five-time-step rRESPA^{38–40} algorithm for MD integration. Bond constraints on hydrogen covalent bonds were used and handled by a Shake–Rattle-like algorithm.^{41,42} All simulations described in this paper were performed with the parallel version of the program ORAC.^{39,40,43}

Calculations of the primary charge separation rate were carried out on the 9600 configurations obtained from the MD trajectory. Conformations were saved with a frequency of 250 fs over the 2.4-ns acquisition run.

B. Electronic Charge Distribution. To make the calculation of the energy gap between charge-transfer states manageable, we used a tight-binding approximation of the wave function of the transferring electron. Thus, electronic states are imagined as being localized on the macro-ring atoms and differ among each other for changes in the electronic density of only a few atoms.

Two different charge distributions on the chromophores atoms were used to model the extra electron (Table 1). In the first, labeled HO, the electron was homogeneously shared among the 16 atoms of the macroring: the 4 nitrogens (N(I), N(II), N(III), and N(IV)) and the 4 methine carbons (C_{α} , C_{β} , C_{γ} , C_{δ}) connecting the 4 imidazol rings and the 8 methine carbons bound to the nitrogens (C1 and C4). The second distribution was derived from ab initio density functional theory (DFT) calculations carried out on the isolated methyl bacteriopheophytin (MeBPheo) *a* molecule. We adopt herein the same naming convention for the atoms of the bacteriochlorophyll and bacteriopheophytin derivatives used in refs 34 and 44.

The level of DFT theory and technique used here is described in previous papers.^{34,44} Briefly, our computations were based on the density functional theory^{45,46} in the local density plus gradient corrections approximation (LDA+GC). Only valence electrons are included explicitly in our computation, and their interaction with the ionic cores is described by ab initio norm-conserving pseudopotentials.⁴⁷ Single-electron orbitals are expanded on a basis of plane waves with a kinetic energy cutoff of 70 Ry. All DFT calculations presented here were run with the CPMD program.⁴⁸

To simulate an excess electron on MeBPheo *a*, a derivative of BPh where the pheophytin chain was replaced by a methyl group, we used a technique due to Frank et al.⁴⁹ that provides a very good approximation for the true electronic states and total energy of the anion. From the geometry-optimized structure of MeBPheo *a* obtained previously,³⁴ an extra electron is first added to the first excited Khon–Sham state of the molecule. The electronic wave functions and, subsequently, the nuclear coordinates of the new anion are then optimized.

In our specific case, wave functions were always optimized by the method of direct inversion in the iterative subspace,^{50,51} and nuclear coordinates were relaxed by the ab initio molecular dynamics method of Car and Parrinello.⁵² From the new electronic density and nuclear coordinates, atomic charges were derived that fit the ab initio electrostatic potential around the molecule.^{53,54} This ESP (electrostatic potential fit) charge

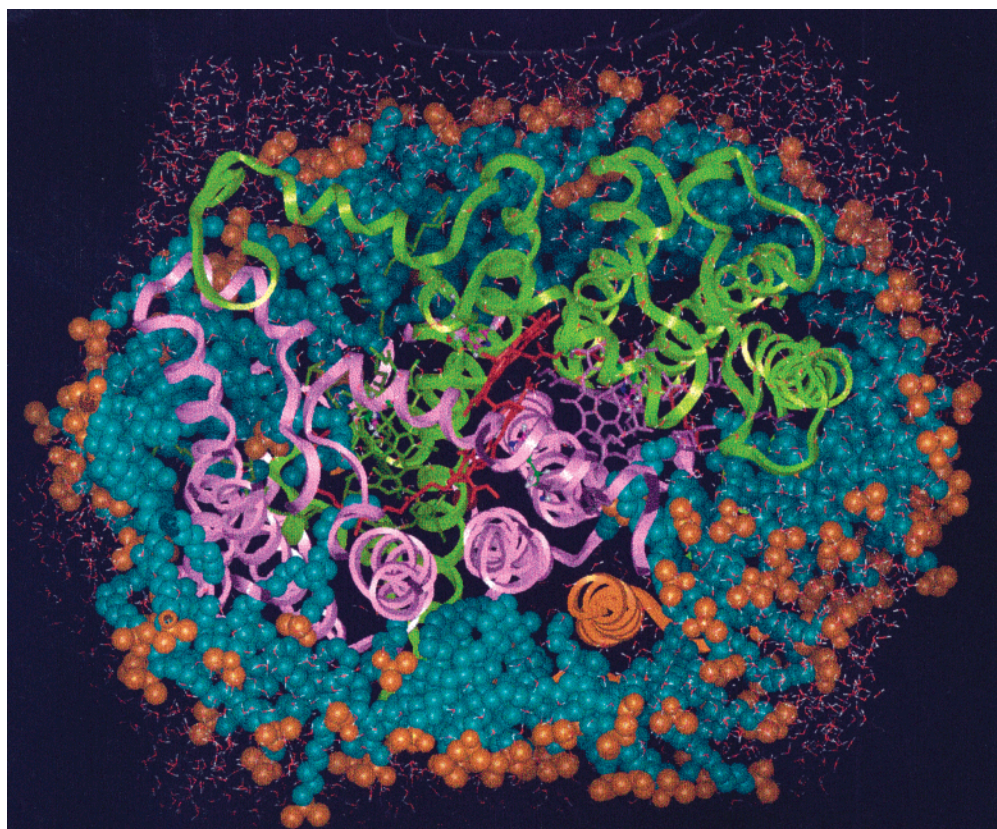


Figure 2. Pictorial representation of the simulated system after 3.4 ns. An instantaneous picture of the simulation box is shown. The plane of the pictures is normal to the quasi- C_2 symmetry axis of the RC protein.

distribution, labeled DFT, is used for both bacteriochlorophylls and bacteriopheophytins. It agrees qualitatively with previous distributions obtained from semiempirical calculations.⁵⁵

Because of computational limitations, we were unable to apply the same DFT approach to the calculation of the special pair charges. Thus, we distributed homogeneously a half electron charge on the 16 macro-ring atoms of each BChl. The distribution on P is also called HO, and it corresponds to the charges in Table 1 scaled by a factor of 0.5. All calculations described here were carried out with the HO distribution on the dimer P and the DFT distribution for the excess electron on the other chromophores.

C. Electronic Polarization. In our model, only electrostatic forces act on the exchanging electron. The dielectric response of the environment—protein, water, and detergent—surrounding the chromophores is due to both nuclear and electronic polarizations. The charge distribution of the electrostatic force field used in our MD simulation, AMBER, accounts for electronic polarizations in a mean-field way. Indeed, although no electronic contributions are explicitly included in the potential, atomic charges on the protein, water, and detergent are effective charges, corrected and scaled for use in condensed-phase simulations.^{53,54,56} In contrast, to compute the primary charge separation activation and reorganization energies and driving force, we explicitly included the electronic polarization in the calculation of the energy gap.

Our model for electronic polarization⁵⁷ assigns a polarizability, α , and a dipole moment, $\vec{\mu}$, to each atom of the system. For a system composed of N atoms, the atomic dipoles are obtained by solving self-consistently the N equations:

$$\vec{\mu}_i = \alpha_i \vec{E}_i(\{q\}^N, \{\vec{\mu}\}^N) \quad (15)$$

Here, the electrostatic field $\vec{E}_i(\{q\}^N, \{\vec{\mu}\}^N)$ is split into two contributions due to charges and to the other dipoles:

$$\vec{E}_i(\{q\}^N, \{\vec{\mu}\}^N) = \vec{E}_i^c(\{q\}^N) + \vec{E}_i^d(\{\mu\}^N) \quad (16)$$

with

$$\vec{E}_i^d(\{\mu\}^N) = \sum_{j \neq i} T_{ij} \vec{\mu}_j \quad (17)$$

where T_{ij} is the dipolar tensor.

In practice, eq 15 was solved by choosing an initial atomic dipole $\vec{\mu}_i^0 = 0$ and iterating the equation

$$\vec{\mu}_i^{n+1} = \alpha_i [\vec{E}_i(\{q\}^N) + \sum_{j \neq i} T_{ij} \vec{\mu}_j^n] \quad (18)$$

For our system and our parametrization (see below), we found that to stop iterating when differences between dipoles at two subsequent steps were smaller than 2×10^{-2} D provided adequate convergence for the calculation of the energy gap and involved at most four iteration steps.

In our calculations, the atomic polarizabilities for the cofactors, protein, detergent, and water were taken from a recent parametrization⁵⁸ of the Thole model⁵⁷ for electronic polarization. This parametrization reproduces the molecular polarizabilities of a set of 52 organic molecules very well and involves a very limited set of parameters, with only one atomic polarizability for each element considered. In Thole's approach, the so-called polarization catastrophe⁵⁹ occurring when short-range dipole–dipole interactions make eq 15 unstable is avoided by smoothing the dipolar tensor below a certain cutoff. For the cofactors, the proteins, and the detergent, we used the new set of polarizabilities corresponding to the exponential smoothing

TABLE 1: Distribution of the Excess Electron on H Calculated with ab Initio Methods^a

atom	HO	DFT	Warshel ⁵⁵
C1	-0.0625	-0.055	-0.086
C2	0.0	-0.079	-0.040
N-I	-0.0625	+0.020	-0.014
C3	0.0	-0.051	-0.036
CO-I	0.0	-0.012	0.00
O-I	0.0	-0.027	0.00
C4	-0.0625	-0.035	-0.120
C α	-0.0625	-0.057	-0.002
subtotal	-0.250	-0.296	-0.298
C1	-0.0625	-0.049	-0.076
C2	0.0	0.000	0.000
N-II	-0.0625	-0.025	-0.013
C3	0.0	0.000	0.000
C4	-0.0625	-0.061	-0.120
C β	-0.0625	-0.056	-0.030
subtotal	-0.250	-0.191	-0.239
C1	-0.0625	-0.054	-0.070
C2	0.0	-0.078	-0.035
N-III	-0.0625	+0.017	-0.017
C3	0.0	-0.037	-0.020
C4	-0.0625	-0.032	-0.094
CO-V	0.0	-0.027	0.00
O-V	0.0	-0.031	-0.005
C γ	-0.0625	-0.067	-0.006
subtotal	-0.250	-0.309	-0.247
C1	-0.0625	-0.044	-0.057
C2	0.0	0.000	0.000
N-IV	-0.0625	-0.035	-0.020
C3	0.0	0.000	0.000
C4	-0.0625	-0.062	-0.108
C δ	-0.0625	-0.063	-0.035
subtotal	-0.250	-0.204	-0.220

^a We define four groups, each corresponding to a different ring, labeling the nitrogen atoms. They are separated by lines. For each, we give the total charges and compare with data from ref 55. C1 and C4 are the atoms bound to the nitrogens, and C2 and C3 are the atoms at the base of the imidazole rings. C atoms with Greek subscripts identify the methine carbons connecting the four imidazole rings, and CO and O are the carboxylic atoms of the acetyl group (ring I) and of the keto group (ring V attached to ring III), respectively. This list of atoms was also used for the electrostatic potential and field representation.

in ref 58. (See Table 2.) For water, the oxygen and hydrogen polarizabilities, respectively labeled OW and HW in Table 2, were adapted by us to TIP3P water. Given that Mg and Fe polarizabilities for the Thole model are not available, we used a value that was 2.5 au smaller than that for C and suitable for nonpolarizable ions. Given that the system contains only four Mg atoms and one Fe atom, changes in these polarizabilities have little effect on the overall induction.

We note that in eq 15 the electrostatic field due to fixed charges, $\vec{E}_i(\{q\}^N)$, is different from the field of our MD simulations. First, the AMBER force field excludes 1–2, 1–3, and, partially, 1–4 interactions from the electrostatic energy. Instead, the parametrizations of Thole's model were carried out including all of these contributions. For consistency, we exclude no neighbors in the dipole–dipole and dipole–charge terms of eq 15. Second, the set of AMBER charges $\{q\}^N$ was derived in the past by ab initio ESP calculations and subsequently scaled homogeneously to account, in a mean-field way, for electronic

polarization. In the past, a value of 0.88–0.90 was proposed to scale ESP charges when polarization effects were treated explicitly.⁵⁹ In our calculations, a factor of 0.8 was used instead. Our smaller value compensates for the larger effects arising from neighbors 1–2 and 1–3 interactions of Thole's model, missing in the scheme used by Caldwell and Kollman in ref 59. In good agreement with experimental values, averaged dipole moments of 2.65 and 2.14 D were obtained for liquid TIP3P water and methanol,⁷¹ respectively, if a scaling factor of 0.8 and the parametrization of ref 58 were used.

To compute the electrostatic field due to charges and dipoles, we used the smooth particle mesh Ewald (SPME) technique described in ref 60. It must be pointed out here that a Ewald approach is essential to obtain convergence not only for $\vec{E}_i(\{q\}^N)$ but also for $\vec{E}_i^d(\{\mu\}^N)$. Attempts to compute the latter contribution with a spherical cutoff failed even at cutoffs as large as 25 Å.

IV. Results

A. Energy Gaps. As shown in section 2, the kinetics of the primary charge separation can be obtained from the averages and fluctuations of the energy gaps between the charge-transfer states along the L and M branches. According to eq 3, the energy gap between states i and j , $\Delta E_{ij}(t)$, is composed of contributions from solvation and the gas phase. The former is obtained from the MD trajectory by taking the electrostatic energy difference between states i and j after the relaxation of their respective electronic polarization (i.e., their atomic dipoles). In our calculation, this energy gap included terms due to the environment but no components due to the cofactors where the excess electron localizes in the current state. Thus, for state P*, or state 1, only electrostatic contributions from the protein, detergent, water, and the remaining cofactors (accessory bacteriochlorophylls and pheophytins) were considered whereas the cofactor internal contributions due to the charges and relaxed dipoles on the special pair were not. In the case of bacteriochlorophylls, our model considered ligand histidines to be part of the environment. Also, the isoprene tails were not considered to be part of the chromophores, and in the gap calculation, the phytol chain was truncated after the ester link but included the methyl group attached to the oxygen. All other atoms of the tails are considered to be the environment. Finally, the P chromophore, although composed of two BChl's, was considered to be one unique cofactor.

The gas-phase contribution is less straightforward to evaluate and implies estimates from sources other than our MD simulations. It is a commonly accepted approximation to take the vertical shift of the paraboloids from quantum chemistry at various level of theory, carried out on the relaxed structure of the cofactor. In our calculation, the energy to ionize P and the electron affinities of B and H were taken from recent literature.¹² These were estimated using ab initio methods (hybrid density functional type). (See Table 3.) Given the large number of atoms in P, its ionization energy was obtained in ref 12 with approximations using the ionization energy of single monomers. Thus, this energy is to be considered less accurate than the others.

We remark here that these values of electron affinities and ionization energies are in agreement with previous calculations

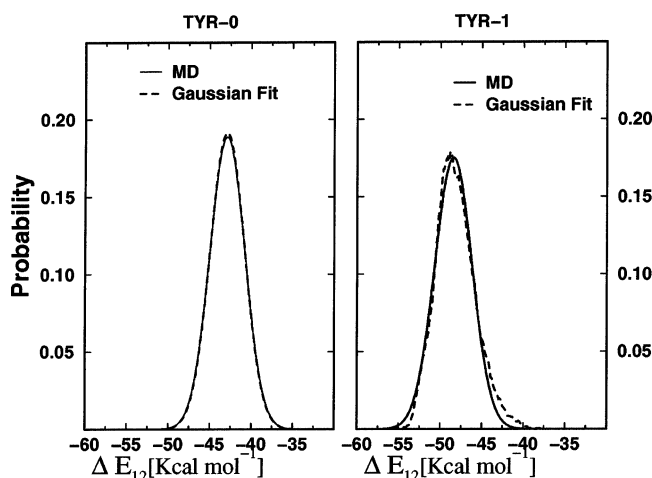
TABLE 2: Atomic Polarizabilities in Atomic Units (au) Used in Our Calculation

atom	H	C	N	O	F	S	OW	HW	Mg	Fe
α (au)	1.385 ^a	6.578 ^a	2.985 ^a	2.318 ^a	1.491 ^a	10.865 ^a	4.454 ^b	1.434 ^b	2.5 ^b	2.5 ^b

^a Values taken from ref 58. ^b This work. An exponential smoothing for the dipole–dipole tensor parametrized in ref 58 was used in both cases.

TABLE 3: Ab Initio Estimates of Ionization Energies and Affinities for the Isolated Chromophores of the *Rb. sphaeroides* RC^a

system	ionization	affinity
P	130.5	
P*	97.5	
BChl		-50.7
BPh		-47.9

^a All energies are in kcal mol⁻¹.¹²**Figure 3.** Gaussian fit of the probability distribution of the energy gap between P* and P+B_LH_L for states labeled Tyr0 (left) and Tyr1 (right). Probabilities are normalized to 1. Only the environmental contribution to ΔE₁₂ is shown here.

based on semiempirical methods and thermodynamic integration.¹⁰ As an extra check, we recomputed the electronic affinity of BPh using the method described in ref 49 and sketched in section 3.2. We found that the difference in total energy between the state with an extra electron and the ground state (i.e., the electronic affinity) fell within a few tenths of 1 kcal mol⁻¹ of the value reported in ref 12.

The electron-transfer theory described in section 2 applies to linearly responding models. In that case, the probability distribution of the energy gap, $P(\Delta E_{ij})$, is Gaussian, and the corresponding free energies are parabolas. Except for ΔE_{ij} involving the accessory bacteriochlorophyll on the L side, the histograms of $P(\Delta E_{ij})$ constructed from the MD trajectory were well fit by single Gaussian functions, with statistical errors of approximately 0.3 kcal mol⁻¹ on ⟨ΔE_{ij}⟩ and 1.0 kcal mol⁻¹ on α_{ij}.

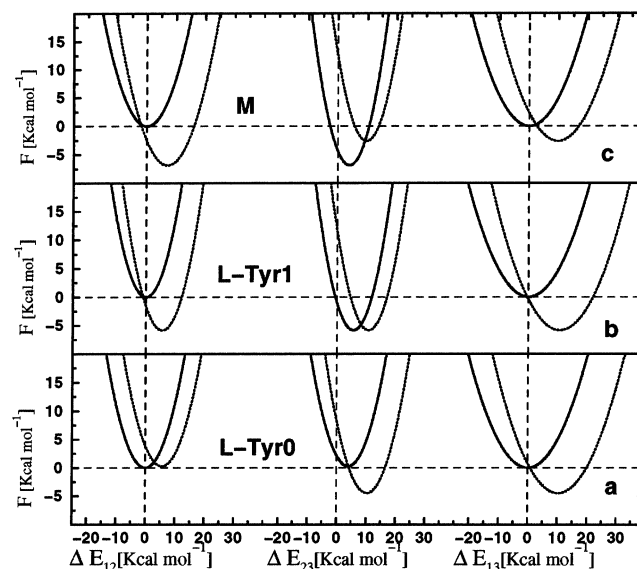
As discussed in a previous paper,²⁹ our simulation finds a bistable state involving Tyr M210: in the first orientation, labeled Tyr0, the Tyr O–H group forms a hydrogen bond with the acetyl oxygen of P_M (7524 configurations out of 9600); in the second, labeled Tyr1, it points toward B_L. It is no surprise that the marked polarity of the Tyr M210 O–H group produces two peaks in $P(\Delta E_{ij})$ involving B_L. The probability distribution of each of these two states can be fit by a Gaussian, and for calculations involving B_L, we split the trajectory into two parts and applied a linear response to states Tyr0 and Tyr1 separately. In Figure 3, we show these distributions. Although the curve for Tyr1 is less Gaussian than that for Tyr0, its statistical noise is larger than for Tyr1. A similar bistable state was also observed by Warshel, Parson, and co-workers.⁶¹

B. Primary Electron Transfer. For the AMBER electrostatic field, we report in Table 4 the kinetic parameters for the primary electron transfer obtained from our MD trajectory. These results are summarized in Figure 4, where we report the free-energy

TABLE 4: Kinetic Parameters for the Primary Electron Transfer in *Rb. sphaeroides* Computed Using the AMBER Atomic Charge Distribution for Amino Acids^a

parameters	exptl	AMBER				
		L-Tyr0	L-Tyr0 ^q	L-Tyr1	M side	Tyr/Phe
α ₁₂		7.22	11.36	8.46	8.70	7.00
α ₁₃		10.38	19.84	10.73	9.74	10.44
α _⊥		5.69	9.46	5.58	7.10	5.36
<i>b</i>		0.384	0.309	0.518	0.405	0.384
Δε ₁₂		3.89	18.81	-1.61	-2.54	1.04
Δε ₁₃		0.74	3.10	-0.48	2.26	0.21
λ ₁₂		3.61	5.68	4.23	4.35	3.50
λ ₂₃		4.81	9.47	4.03	5.27	4.58
λ ₁₃		5.19	9.92	5.36	4.87	5.22
ΔG ₁₂ ⁰	-1.5 ^b	0.29	13.13	-5.84	-6.89	-2.45
ΔG ₂₃ ⁰		-4.74	-19.95	0.00	4.28	-2.56
ΔG ₁₃ ⁰	-5.8 ^c	-4.45	-6.82	-5.84	-2.60	-5.01
G ₁₂ [*]	0.0	1.05	15.58	0.15	0.37	0.01
G ₂₃ [*]	0.0	0.00	2.90	1.00	4.33	0.22
G ₁₃ [*]	0.0	0.03	0.24	0.01	0.26	0.00

^aAll energies are in kcal mol⁻¹. Column labels L-Tyr0 and L-Tyr1 refers to the kinetic parameters of the L side for the two states of Tyr M210 as described in the text. In turn, M side and Tyr/Phe label the kinetic parameters for the M side and for the Tyr/Phe “static” mutation. No electronic polarization contribution was included in the results labeled L-Tyr0^q. Finally, symbols on the first column are fully explained in section 2. ^b Experimental driving force taken from ref 15. ^c Experimental driving force taken from ref 70.

**Figure 4.** Pictorial representation of the free-energy parabolas for the primary charge separation in *Rb. sphaeroides*. From left to right, in each of three panels we present the free-energy surfaces for the transfers from states P* → P+B⁻H, P+B⁻H → P+BH⁻, and P* → P+BH⁻, respectively. The solid and dotted lines are the initial and final states, respectively. Panel c presents the free energy parabolas for the electron transfer on the M side. Results depicted in panels a and b are for the L side in conformational states L-Tyr0 and L-Tyr1, respectively.

curves for the primary charge separation on both the L and M sides. In addition, in Table 5, we present results obtained by using the CHARMM⁶² electrostatic model for the protein in the analysis of the trajectory.

In both CHARMM and AMBER, the statistics used to obtain driving forces and reorganization energies are 5–10 times larger than in previous work, with corresponding statistical errors of 0.8 and 0.5 kcal mol⁻¹, respectively. It must be stressed that all of our results were obtained without any a posteriori

TABLE 5: Kinetic Parameters for the Primary Electron Transfer in *Rb. sphaeroides* Computed Using the CHARMM Atomic Charge Distribution for Amino Acids^a

quantity	exptl	CHARMM		
		L-Tyr0	L-Tyr1	M side
α_{12}		7.30	8.88	9.08
α_{13}		8.84	9.72	9.70
α_{\perp}		5.54	5.55	7.39
b		0.4475	0.5851	0.4188
$\Delta\epsilon_{12}$		3.06	-2.80	-2.31
$\Delta\epsilon_{13}$		-1.55	-2.97	2.63
λ_{12}		3.65	4.44	4.54
λ_{23}		4.12	3.61	5.33
λ_{13}		4.42	4.86	4.85
ΔG_{12}^0	-1.5	-0.60	-7.23	-6.85
ΔG_{23}^0		-5.37	-0.60	4.63
ΔG_{13}^0	-5.8	-5.97	-7.83	-2.22
G_{12}^*	0.0	0.64	0.44	0.29
G_{23}^*	0.0	0.10	0.63	4.65
G_{13}^*	0.0	0.14	0.45	0.36

^a See Table 4 and text for explanations.

renormalization procedures, as was done in earlier simulations.⁹ In addition, since our molecular and electrostatic modeling is atomistically based, no artificial boundaries for the protein and both nuclear and electronic polarizations need to be set as in previous work.^{10,28,55}

1. L-Side Energetics. Keeping in mind the computational uncertainties of the gas-phase energy gap, we find remarkable agreement between our driving forces in Table 4 and the experiment. Similar good agreement is also found for the corresponding kinetic parameters obtained with the CHARMM charges in Table 5. Indeed, by comparing Tables 4 and 5, we find that changes in ΔG_{ij}^0 between the two charge models never exceed 2 kcal mol⁻¹; smaller differences (<0.7 kcal mol⁻¹) are found for the reorganization energies. In particular, for AMBER the largest deviation of ΔG_{13}^0 is for state Tyr0, which is less negative by 1.35 kcal mol⁻¹, whereas for CHARMM, state Tyr1 gives a driving force more negative by about 2 kcal mol⁻¹.

Not surprisingly, larger deviations in the driving forces ΔG_{12}^0 are found between states Tyr0 and Tyr1 for both AMBER and CHARMM. In the case of Tyr0, the P⁺B_LH_L state is found 0.3 kcal mol⁻¹ above P* for AMBER and 0.6 kcal mol⁻¹ below for CHARMM. For both charge models, Tyr1 stays well below P* and very close to P⁺B_LH_L⁻. To compare with experiment, the weighted average of ΔG_{12}^0 was obtained by adding the average driving forces in the Tyr0 and Tyr1 states multiplied by their probability of occurrence in our simulation. Such estimates are in good agreement with experimental values obtained for modified RCs (ca. -1.5 kcal mol⁻¹) and give -0.72 kcal mol⁻¹ for AMBER and -1.69 kcal mol⁻¹ for CHARMM.

All of the reorganizational energies are very close to one another—almost within statistical error—for the two charge models. Consistently, in the two cases, λ_{12} for state Tyr0 is always smaller than that for Tyr1. This is to be related to the more rigid and stronger interaction experienced by the O—H group of Tyr M210 forming a hydrogen bond in state Tyr0.

According to our calculation, all of the three possible electron exchanges are always close to being activationless. For both AMBER and CHARMM substates, Tyr0 has higher activation energies for the P* → P⁺B_LH_L transfer; these are 1 and 0.6 kcal mol⁻¹, respectively. Tyr1 instead involves a higher activation for P⁺B_LH_L → P⁺B_LH_L⁻, with 1 kcal mol⁻¹ for AMBER and 0.63 kcal mol⁻¹ for CHARMM.

Finally, we turn on the effect of electronic polarization on electron transfer. In the third and fourth columns of Table 4, we report the L-side kinetic parameters obtained with the AMBER electrostatic field modified to include bare charges or electronic polarization, respectively. The most significant effect of atomic dipoles is an almost 50% reduction in the reorganization energy, λ_{ij} , and thus in the energy-gap fluctuations. In addition, electronic polarization stabilizes state P⁺B_LH_L to a very large extent by reducing the driving force ΔG_{12}^0 by 12.84 kcal mol⁻¹, whereas smaller effects are instead observed for the P⁺B_LH_L⁻ state. These results are in agreement with previous findings of Warshel and Parson's groups,^{10,28} which predicted large polarization effects on the accessory bacteriochlorophyll on the L side.

2. M-Side Energetics. Although for the inactive side no experimental records are available for the wild-type RC of *Rb. sphaeroides*, our calculation arrives yet again at a consistent picture for the two charge distributions, AMBER and CHARMM. We find that ΔG_{12}^0 is more negative in value than its counterpart on the L side, and ΔG_{23}^0 and ΔG_{13}^0 on the M side are markedly higher. In particular, ΔG_{23}^0 and the corresponding activation energy G_{23}^* are found to be positive and larger than 4 kcal mol⁻¹. This result energetically positions the accessory BChl on the M side below P*, in striking contrast to the result for the active branch. On the contrary, consistently for AMBER and CHARMM, we find reorganization energies very close—almost within statistical uncertainty—to those of the L side. Because reorganization energies can be related directly to the dielectric response of the media to electron transfer, our calculation does not identify any detectable dielectric asymmetry between the active and inactive branches.

3. “Static” Tyr/Phe M210 Mutation. Given that our simulation found a bistable state involving Tyr M210, we have investigated the effect of mutation on a nonpolar amino acid at this location. To perform what we call a static mutation of Tyr M210 to Phe, for each configuration of the MD trajectory the Tyr O—H group is transformed by one hydrogen placed at the position of the original oxygen. With the new coordinates and after replacing the Tyr charges with those of Phe, we recalculated the kinetic parameters shown in Table 4. We stress that all structural and dynamic relaxation of the system due to a “real” mutation is missed in this approach. Indeed, even small systematic changes in interatomic distances of atomic charges have important effects on energy gaps. Thus, we consider this to be a way of removing the barrier between the Tyr0 and Tyr1 states, not of simulating “real” mutations.

The major effect of this static mutation is to change markedly the driving forces involving state 2 (P⁺B_LH_L) as compared to results for both the Tyr0 and Tyr1 states. Indeed, ΔG_{12}^0 and ΔG_{23}^0 , computed to be -2.45 and -2.56 kcal mol⁻¹, respectively, have intermediate values between the driving forces of the two wild-type states. At the same time, ΔG_{13}^0 and all of the reorganization energies are little affected by the mutation. Finally, this mutation also lowers the activation energy of the P* → P⁺B_LH_L electron exchange to about 0 kcal mol⁻¹.

4. Asymmetry. To gain further insight into the functional asymmetry of the RC, we supplemented our investigation of the kinetic parameters of both branches with one additional calculation where we probed the electrostatic potential on the RC cofactors. This potential does not include contributions from inside the cofactors but accounts only for solvent effects due to the environment—protein, detergent, and water.

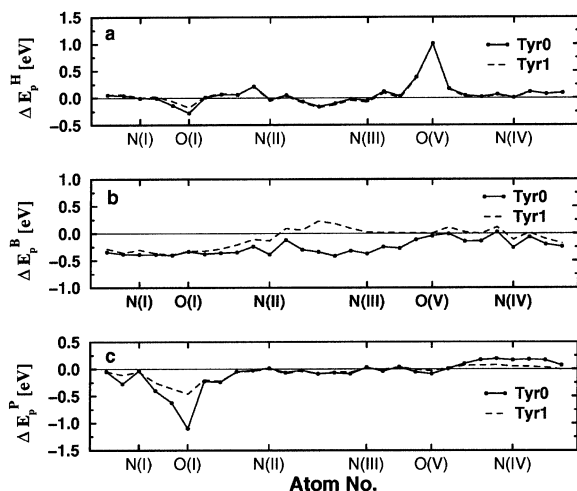


Figure 5. Electrostatic potential differences between chromophore atoms of the active and inactive sides. For the atoms of the chromophores, we used the naming convention of refs 34 and 44. See the text for further details

In Figure 5, we present differences in the average electrostatic potential, or ΔE_p^X , between the atoms of the three couples of chromophores on active (L) and inactive (M) branches. For any type of chromophore X, ΔE_p^X is given by the difference $\Delta E_p^X = E_p^{X_M} - E_p^{X_L}$ where $E_p^{X_M}$ and $E_p^{X_L}$ are the electrostatic energies computed on the corresponding atom of chromophore X on the M and L sides, respectively. ΔE_p , averaged over the entire trajectory, was computed with the AMBER charges and includes contributions from electronic and nuclear polarizations. In each of the panels, the positive value of ΔE_p means that the electron has a lower energy when staying on the L side. Its negative value implies instead a preference for the M side.

We first focus on the differences between ΔE_p values of the Tyr0 and Tyr1 substates. Not surprisingly, changes in the Tyr O–H orientation influence only ΔE_p^P and ΔE_p^B in parts of the chromophores that are more likely to bond to that group. For P, this region is near the acetyl group, whereas the region of ring II and ring III is most affected for B_L (panels b and c of Figure 5). We also notice that ΔE_p^B changes signs for atoms in the region of rings II and III.

Concerning the BPh's, a localized asymmetry favoring the L side is present near and about the keto oxygen of the Vth ring, O(V) (panel a). This asymmetry is related to the presence near O(V) of the protonated Glu L104. We stress, however, that the effects of Glu L104 on electron-transfer properties are not as important as they might seem from panel a. Indeed, the wave function of the excess electron is likely to be delocalized on the imidazol ring of the bacteriopheophytin⁶³ and *not* on the keto oxygen O(V). We remark that single-point mutations of this residue did not change the kinetic primary charge separation significantly.⁶⁴

More significantly, ΔE_p^B presents a strong asymmetry in a large region from ring I through ring II (panel b in Figure 5). Because this region is more likely to be visited by the excess electron on P^* , its effect on the electron-transfer properties is larger than that of the asymmetry on the BPh's. As mentioned earlier, the potential asymmetry for atoms from N(II) to N(IV) is due to the bond between Tyr M210 and the methine carbon. Instead, in the region from N(I) to N(II), differences in the hydrogen bonding of the acetyl group, O(I), cause the asymmetry.

Finally, near ring I in the region from N(I) to O(I), ΔE_p^P is negative and shows an important minima for both Tyr0 and

TABLE 6: Estimates of the Primary Electron-Transfer Rates for the Wild Type of *Rb. sphaeroides* Obtained from Superexchange and Two-Step Mechanisms^a

system	superexchange	two-step		
	τ [ps]	k_{12} [ps^{-1}]	k_{23} [ps^{-1}]	τ [ps]
Tyr0	174	0.133	8.392	7.6
Tyr1	25	0.551	1.690	2.4
Tyr-Phe	11.8	0.688	5.909	1.6
M side	1216.0	0.116	3.D-3	

^a See the text for details.

Tyr1 (panel c). This means that the excess electron is polarized on the M side of P in one of its region closest to B_L , at an averaged contact distance during our MD simulation of 4.80 Å. We remind the reader that in the crystallographic structure and in our simulation P_L is closer to B_M but P_M is closer to B_L . The minimum in O(I) is deeper for state Tyr0 than for state Tyr1. We point out that because ΔE_p^P is a measure of the electrostatic asymmetry acting on the excess electron of the special pair it signals an environment-induced polarization of the electron in the region near O(I). This is likely to affect significantly the electronic coupling between the P and the accessory bacteriochlorophyll on the L side.

V. Kinetics of Electron Transfer

Equations 10 and 11 can be used to compute the rate constants for the primary charge separation in the RC's active and inactive branches. All of the parameters of these equations have been determined from our molecular modeling, except electronic coupling matrix elements V_{12} and V_{23} of the two branches. We point out that V_{13}^s can be estimated from the two former couplings and our averaged energy gaps according to eq 14. Thus, in Table 6 we present electron-transfer rates obtained with our kinetic parameters obtained from the AMBER charge distribution and the electronic coupling term derived by Friesner et al.¹³ for the RC of *Bl. viridis*. Specifically, we used $V_{12} = 34.45$ and 19.1 cm^{-1} and $V_{23} = 122.17$ and 95.45 cm^{-1} for the L and M sides, respectively. Given the computational uncertainty, our rates can be used only to compare the relative efficiency of the electron-transfer channels.

We first notice that the two rate constants computed for the two-step mechanism at 300 K for state Tyr0 and Tyr1 are 7.6 and 2.4 ps, respectively, which is within the range of the experimental value of ~ 3 ps. Superexchange instead provides larger relaxation times of 174 ps for Tyr0 and 25 ps for Tyr1, and at 300 K, it is not competitive with the two-step mechanism. Nevertheless, although the superexchange rates are smaller than those given by the two-step mechanism, they are temperature-independent because the transition $P^* \rightarrow P^+B_LH_L^-$ is activationless in our modeling. Indeed, because of barriers of $\sim 1 \text{ kcal mol}^{-1}$ for steps $P^* \rightarrow P^+B_L^-H_L$ of Tyr0 and $P^+B_L^-H_L \rightarrow P^+B_LH_L^-$ of Tyr1, at 100 K the time constants computed for the two-step mechanism are 115 and 12 ps larger than experimental estimates, respectively.

Because of the uncertainties of our calculation, it is useful to analyze the dependence of our kinetic results from the parameters. As a test, for the AMBER results of Tyr0 we have shifted down the positions of the intermediate and final states of $1.3 \text{ kcal mol}^{-1}$ to fit the driving force $P^* \rightarrow P^+B_LH_L^-$ to the experimental value of $-5.8 \text{ kcal mol}^{-1}$ exactly. We find that although the two-step mechanism gives a value of 2.6 compared to 7.6 ps, for the superexchange we go from 174 to 97 ps. We notice, however, that the coupling matrix element for superexchange is very close to its resonance, which corresponds to small

values of the denominator in eq 14. With further changes of 1–2 kcal mol⁻¹ in the position of P* we obtain an increasingly stronger superexchange channel for ET. This channel clearly takes over for the substate Tyr1 if P* is lowered by 1.3 Kcal mol⁻¹, with a decay rate in the femtosecond range (0.01 ps).

Thus, our molecular modeling positions the diabatic free-energy surfaces for the primary electron transfer very near the resonance region of the superexchange coupling between P* and P⁺B_LH_L. Given the small changes in driving force shown to favor the superexchange mechanism, our surfaces are not sufficiently accurate to distinguish clearly between the two possible mechanisms. Indeed, despite the precision of our statistical mechanics results, inaccuracies in the ab initio gas-phase energies of the chromophores and in our modeling of nuclear and electronic polarization are very likely to produce uncertainties of at least a few kcal mol⁻¹.

In summary, our molecular modeling predicts for the primary charge separation on the L side a wide variety of temperature-dependent relaxation times from 2 to 200 ps. This multiexponential behavior, which has been pointed out experimentally,²⁰ is related in our modeling to isomerizations involving Tyr M210 and to the two possible mechanisms that might coexist over a wide range of conformational parameters and temperatures.

Finally, our calculation predicts that state P⁺B_M⁻H_M is lower than P* with a driving force of about -7 kcal mol⁻¹ (see Tables 4 and 5 and Figure 4). We stress that our calculations with both AMBER and CHARMM charges always predict driving forces and activation energies on the M side within a few tens of kcal mol⁻¹ of each other. The presence of water molecules or detergent headgroups within close range of B_M could have an important effect on this findings. However, in agreement with the structural results of our simulation, to our knowledge, there is no experimental evidence of polar molecules near this cofactor. As a consequence, given the good representation of the energetics on the L side, we think that errors in the solvation contribution to the driving force for P* → P⁺B_M⁻H_M are unlikely to account for the energetic position of B_M vis-à-vis P.

Meanwhile, we assumed the same electronic affinity for B_M and B_L. X-ray structures carried out by different groups have shown a large uncertainty in the orientation of the carbonyl of the acetyl group. In Ermler's structure⁶⁵ used in our investigation, the carbonyl oxygen of B_L is oriented toward the imidazol ring, and in B_M, it is oriented toward its terminal methyl group. In other X-ray structures,⁶⁶ the same group on both B components is oriented outside the ring. Given the polarity of this group, its orientation might significantly shift the gas-phase energy of B_M vis-à-vis B_L.

With the electronic couplings used to compute the data in Table 6, the electron exchange would take place on the M side rather than on the L side from P* to B_M. In the past, quantum chemistry calculations of the coupling matrix element for the primary charge transfer in RCs have been plagued by the large uncertainty in the results due to the heavy approximations in the theory used to treat such large systems. In all of the investigations carried out so far,^{13,14} the effect due to the environment was included by adding a few amino acids to the cofactors of the calculations. The effects due to the environment that can polarize the excess electron state are not taken into account fully. Indeed, in the past, it was suggested that an asymmetric electronic distribution could be the source of the inactivity of the M side.^{13,14} A change in our electronic density on P—in our modeling, we used a homogeneous distribution for the exchange that was equally “distributed” on the two

monomers of P—would affect only the reactant state, changing the energies on both sides by the same amount. However, an asymmetric distribution has an important effect on the electronic coupling term. We have shown in section 4.2.4 that the electrostatic potential favors a polarization of the electron on the M monomer near acetyl group O(I) (See Figure 5. This group is also the closest to B_L.)

Because electronic coupling is directly proportional to the distances between the edges of the cofactors, our results suggest that the asymmetry in the electronic coupling might play a significant role in the functional asymmetry of RCs. From the experimental point of view, no single mutations of the amino acid chains ever produced a change in the activity of the two sides. Only three point mutations⁴ and β-type mutations^{5–7} were able to produce branching to the M side. Indeed, chromophores such as bacteriochlorophylls and pheophytins are very rigid in the RC protein complex,²⁹ and only large structural changes might modify their mutual positions and affect the electronic coupling term.

VI. Summary and Conclusions

This paper has focused on the molecular modeling of the primary electron transfer in the *Rb. sphaeroides* reaction center. The kinetic parameters for the electron transfer along the active (L) and inactive (M) sides were obtained from a long MD trajectory of the RC in an amphiphilic environment of detergent molecules and water. In this calculation, electronic and nuclear polarizations were included explicitly, and two different sets of atomic charges for the protein were used. For both AMBER, which was also used in the MD simulation, and CHARMM charges, we were able to compute from first principles the driving forces for the transfer of the excess electron to B_L and H_L from P* in good agreement with experimental estimates.

For the active branch, two conformational states of Tyr M210 affect the kinetics of the primary charge separation both for sequential (two-step) and superexchange mechanisms. Thus, on the L side, the kinetics of the primary charge separation is multiexponential, as found experimentally,²⁰ and has four characteristic times for the decay of the P* state due to both conformational heterogeneity and the two possible channels. Using quantum chemistry estimates of electronic coupling,¹³ at room-temperature we find that the two-step channel is favored over superexchange with decay rates of 2.6 and 7.6 ps for substates Tyr0 and Tyr1 whereas superexchange decays are at 25 and 174 ps. However, although the activation energy for superexchange is close to zero, the P* → P⁺B_L⁻H_L step is an activated process by almost 1 kcal mol⁻¹. This activation energy is not far from that estimated from the time-resolved spectroscopy of *Rb. sphaeroides* mutants at 300 K.¹⁷ However, our molecular modeling with the coupling matrix elements of ref 13 cannot explain the temperature dependence of the primary charge separation rate, which increases with decreasing temperature.

It is important to emphasize that given the proximity between the diabatic free-energy surfaces on the L side the superexchange coupling computed from our modeling is very near its resonance point. Small changes in the positions of the free energies (1–2 kcal mol⁻¹) have large effects on this ET channel, and in certain cases, superexchange might take over the two-step mechanism. The uncertainties that are intrinsic to our approach make discriminating between the two mechanisms difficult at this stage.

With the electronic coupling of ref 13, electron transfer along the inactive branch has a time constant of 8.6 ps and becomes

competitive with that on the L side, even if the electron stops at B_M. The reader should notice, however, that effects due to the protein field on the chromophores were not taken into account in the electronic coupling estimates used here. Indeed, our modeling has shown a strong electrostatic potential around the special pair favoring a polarization of the transferring electron toward regions closer to B_L than to B_M. This polarization should significantly increase the electronic coupling between P* and B_L, thus accounting, at least in part, for the directionality of the initial electron transfer. Thus, our finding that the Franck–Condon parameters for L and M favor competitive branching is an indication, albeit indirect, that the ET asymmetry is due to electron coupling, *not* to coupling with nuclear coordinates.

Concerning the M-side electron transfer, although we compute P⁺B_L[−]H_L to be always within less than 1 kcal mol^{−1} of P*, P⁺B_M[−]H_M is instead lower than P* by about 6.8 kcal mol^{−1} and also lower than P⁺B_M[−]H_M for both atomic charge models. This finding does not explain the results from β-type and triple point mutants that show M-side electron transfer with the electron found on H_M not on B_M.^{5,6} However, we point out that the position of P⁺B_M[−]H_M vis-à-vis P* is an issue far from being settled experimentally. Indeed, in a recent paper by the Woodbury group,⁶⁷ the histidine ligand of B_M RC from *Rb. sphaeroides* was replaced with a glutamic acid residue producing P⁺B_M[−]H_M rather than charge separation on the M side, as in our theoretical investigation. Work is in progress in our group to find the absolute position of B_M in this mutant. We also point out that our results were obtained using the same electron affinity for B_L and B_M. Different orientations of the polar acetyl group of B on the two sides have been revealed in X-ray structures and might be causing a significant shift in the affinity. DFT ab initio calculations are underway to quantify this effect.

Finally, our modeling shows that no significant asymmetry in the reorganization energy and, therefore, in the linear response of the dielectric exists between the two sides. Such a dielectric difference has been invoked many times in the past to explain the inactivity of the M side. (See, for instance, ref 68.)

To conclude, the results of our molecular modeling strongly indicate that the position of the diabatic free-energy surfaces for the primary charge separation cannot by itself account for the directionality of the primary charge separation. Thus, further investigations of the electronic coupling matrix elements need to include an improved representation of the electrostatic effects on the RC chromophores due to the protein, amphiphile, and solvent environments.

Acknowledgment. M.C. was supported by a 3 year individual Marie Curie grant, contract no. ERBFMBICT983309 held at CECAM/ENS-Lyon, France. We are very gratefully to Tom Darden for providing us with a copy of his SPME routine for dipolar interactions prior to publication.

References and Notes

- (1) Kuznetsov, A.; Ulstrup, J. *Electron Transfer in Chemistry and Biology*. Wiley Series in Theoretical Chemistry; Wiley and Sons: New York, 1999.
- (2) Deisenhofer, J.; Epp, O.; Miki, K.; Huber, R.; Michel, H. *J. Mol. Biol.* **1984**, *180*, 385.
- (3) Chang, C.; Tiede, D.; Tang, J.; Smith, U.; Norris, J.; Schiffer, M. *FEBS Lett.* **1986**, *205*, 82.
- (4) Kirmaier, C.; Weems, D.; Holten, D. *Biochemistry* **1999**, *38*, 11516.
- (5) Katilius, E.; Turanchik, T.; Lina, S.; Taguchi, A.; Woodbury, N. *J. Phys. Chem B* **1999**, *103*, 7386.
- (6) Katilius, E.; Katiliene, Z.; Lin, S.; Taguchi, A.; Woodbury, N. *J. Phys. Chem B* **2002**, *106*, 1472.
- (7) Heller, B.; Holten, D.; Kirmaier, C. *Science* **1995**, *269*, 940.
- (8) Chandler, D. In *Classical and Quantum Dynamics in Condensed Phase Simulations*; Berne, B., Ciccotti, G., Coker, D., Eds.; World Scientific: Singapore, 1998; pp 29–49.
- (9) Marchi, M.; Gehlen, J.; Chandler, D.; Newton, M. *J. Am. Chem. Soc.* **1993**, *115*, 4178.
- (10) Alden, R. G.; Parson, W. W.; Chu, Z. T.; Warshel, A. *J. Am. Chem. Soc.* **1995**, *117*, 12284.
- (11) Gunner, M. R.; Nicholls, A.; Honig, B. *J. Phys. Chem.* **1996**, *100*, 4277.
- (12) Blomberg, M. R. A.; Siegbahn, P. E. M.; Babcock, G. T. *J. Am. Chem. Soc.* **1998**, *120*, 8812.
- (13) Zhang, L.; Friesner, R. *Proc. Natl. Acad. Sci. U.S.A.* **1998**, *95*, 13603.
- (14) Kolbasov, D.; Scherz, A. *J. Phys. Chem B* **2000**, *104*, 1802.
- (15) Shuvalov, V. A.; Yakovlev, A. G. *Membr. Cell. Biol.* **1998**, *12*, 563.
- (16) Roberts, J. A.; Holten, D.; Kirmaier, C. *J. Phys. Chem. B* **2001**, *105*, 5575.
- (17) Haffa, A. L. M.; Lin, S.; Katilius, E.; Willias, J. C.; Taguchi, A. K. W.; Allen, J. P.; Woodbury, N. W. *J. Phys. Chem. B* **2002**, *106*, 7376.
- (18) Fleming, G. R.; Martin, J. L.; Breton, J. *Nature* **1988**, *333*, 190.
- (19) Kirmaier, C.; Cua, A.; He, C.; Holten, D.; Bocian, D. *J. Phys. Chem B* **2002**, *106*, 495.
- (20) Beekman, L.; van Stokkum, I.; Monshouwer, R.; Rijnders, A.; McGlynn, P.; Visschers, R.; Jones, M.; van Grondelle, R. *J. Phys. Chem.* **1996**, *100*, 7256.
- (21) Pelloquin, J. M.; Williams, J. C.; Lin, X.; Alden, R. G.; Taguchi, A. K. W.; Allen, J. P.; Woodbury, N. W. *Biochemistry* **1994**, *33*, 8089.
- (22) Hamm, P.; Gray, K. A.; Oesterheld, D.; Feick, R.; Scheer, H.; Zinth, W. *Biochim. Biophys. Acta* **1993**, *1142*, 99.
- (23) Chandler, D. In *Classical and Quantum Dynamics in Condensed Phase Simulations*; Berne, B., Ciccotti, G., Coker, D., Eds.; World Scientific: Singapore, 1998; pp 4–23.
- (24) Treutlein, H.; Schulten, K.; Deisenhofer, J.; Michel, H.; Brunger, A.; Karplux, M. In *The Photosynthetic Bacterial Reaction Center: Structure and Dynamics*; Breton, J., Vermeiglio, A., Eds.; Plenum Press: London 1988; p 139.
- (25) Treutlein, H.; Schulten, K.; Deisenhofer, J.; Michel, H.; Brunger, A.; Karplux, M. *Proc. Natl. Acad. Sci. U.S.A.* **1992**, *89*, 75.
- (26) Warshel, A.; Parson, W. W. *Q. Rev. Biophys.* **2001**, *34*, 563.
- (27) Souaille, M.; Marchi, M. *J. Am. Chem. Soc.* **1997**, *119*, 3948.
- (28) Warshel, A.; Chu, Z.-T.; Parson, W. W. *J. Photochem. Photobiol., A* **1994**, *82*, 123.
- (29) Ceccarelli, M.; Marchi, M. *J. Phys. Chem. B* **2003**, *107*, 1423.
- (30) Marcus, R. A. *J. Chem. Phys.* **1956**, *24*, 966.
- (31) Marcus, R. A. *J. Chem. Phys.* **1956**, *24*, 979.
- (32) Marcus, R. A.; Sutin, N. *Biochim. Biophys. Acta* **1985**, *811*, 265.
- (33) Marcus, R. A. *R. Mod. Phys.* **1993**, *65*, 599.
- (34) Ceccarelli, M.; Procacci, P.; Marchi, M. *J. Comput. Chem.* In press, 2002.
- (35) Cornell, W. D.; Cieplak, P.; Bavy, C. I.; Gould, I. R.; Merz, K. M., Jr.; Ferguson, D. M.; Spellmeyer, D. C.; Fox, T.; Caldwell, J. W.; Kollmann, P. *J. Am. Chem. Soc.* **1995**, *117*, 5179.
- (36) Jorgensen, W. L.; Chandrasekhar, J.; Madura, J. D.; Impey, R. W.; Klein, M. L. *J. Chem. Phys.* **1983**, *79*, 926.
- (37) Essmann, U.; Perera, L.; Berkowitz, M. L.; Darden, T.; Lee, H.; Pedersen, L. G. *J. Chem. Phys.* **1995**, *103*, 8577.
- (38) Tuckerman, M. E.; Berne, B.; Martyna, G. J. *J. Chem. Phys.* **1992**, *97*, 1990.
- (39) Procacci, P.; Darden, T.; Marchi, M. *J. Phys. Chem.* **1996**, *100*, 10464.
- (40) Marchi, M.; Procacci, P. *J. Chem. Phys.* **1999**, *108*, 5194.
- (41) Ryckaert, J. P.; Ciccotti, G.; Berendsen, H. J. C. *J. Comput. Phys.* **1977**, *23*, 327.
- (42) Andersen, H. J. *Comput. Phys.* **1983**, *52*, 24.
- (43) Procacci, P.; Paci, E.; Darden, T.; Marchi, M. *J. Comput. Chem.* **1997**, *18*, 1848.
- (44) Ceccarelli, M.; Lutz, M.; Marchi, M. *J. Am. Chem. Soc.* **2000**, *122*, 3532.
- (45) Parr, R. G.; Yang, W. *Density Functional Theories of Atoms and Molecules*; Oxford University Press: Oxford, U.K., **1989**.
- (46) Jones, R. O.; Gunnarsson, O. *Rev. Mod. Phys.* **1989**, *61*, 689.
- (47) Troullier, N.; Martins, J. L. *Phys. Rev. B* **1991**, *43*, 1993.
- (48) Hutter, J. *CPMD*, program version 3.0; Technical report; Max Planck Institut für Festkörperforschung and IBM Research: 1990–1999.
- (49) Frank, I.; Hutter, J.; Marx, D.; Parrinello, M. *J. Chem. Phys.* **1998**, *108*, 4060.
- (50) Császár, P.; Pulay, P. *J. Mol. Struct.* **1984**, *114*, 31.
- (51) Hutter, J.; Lüthi, H. P.; Parrinello, M. *Comput. Mater. Sci.* **1994**, *2*, 244.
- (52) Car, R.; Parrinello, M. *Phys. Rev. Lett.* **1985**, *55*, 2471.
- (53) Besler, B.; Merz, K.; Kollman, P. J. *Comput. Chem.* **1990**, *11*, 431.

- (54) Bayly, C.; Cieplak, P.; Cornell, W. D.; Kollman, P. A. *J. Phys. Chem.* **1993**, *97*, 10269.
- (55) Parson, W. W.; Chu, Z. T.; Warshel, A. *Biochim. Biophys. Acta* **1990**, *1017*, 251.
- (56) St-Amant, A.; Cornell, W. D.; Halgren, T. A.; Kollman, P. A. *J. Comput. Chem.* **1995**, *16*, 1483.
- (57) Thole, B. T. *Chem. Phys.* **1981**, *59*, 341.
- (58) van Duijnen, P. T.; Swart, M. *J. Phys. Chem A* **1998**, *102*, 2399.
- (59) Caldwell, J. W.; Kollman, P. A. *J. Phys. Chem.* **1995**, *99*, 6208.
- (60) Toukmaji, A.; Sagui, C.; Board, J.; Darden, T. *J. Chem. Phys.* **2000**, *113*, 10913.
- (61) Alden, R. G.; Parson, W. W.; Chu, Z. T.; Warshel, A. *J. Phys. Chem.* **1996**, *100*, 16761.
- (62) MacKerell, A. D., Jr.; Bashford, D.; Bellot, M.; Dunbrack, R. L., Jr.; Evanseck, J. D.; Field, M. J.; Fischer, S.; Gao, J.; Guo, H.; Ha, S.; Joseph-McCarthy, D.; Kuchnir, L.; Kuczera, K.; Lau, F. T. K.; Mattos, C.; Michnick, S.; Ngo, T.; Nguyen, D. T.; Prodhom, B.; Reiher, W. E., III; Roux, B.; Schlenkrich, M.; Smith, J. C.; Stote, R.; Straub, J.; Watanabe, M.; Wiorkiewicz-Kuczera, J.; Yin, D.; Karplus, M. *J. Phys. Chem B* **1998**, *102*, 3586.
- (63) Marchi, M.; Hutter, J.; Parrinello, M. *J. Am. Chem. Soc.* **1996**, *118*, 7847.
- (64) Bylina, E.; Kirmaier, C.; McDowell, L.; Holten, D.; Youvan, D. *Nature* **1988**, *336*, 182.
- (65) Ermler, U.; Fritzsche, G.; Buchanan, S.; Michel, H. *Structure* **1994**, *2*, 925.
- (66) Camara-Artigas, A.; Brune, D.; Allen, J. P. *Proc. Natl. Acad. Sci. U.S.A.* **2002**, *99*, 11055.
- (67) Katilius, E.; Katiliene, Z.; Lin, S.; Taguchi, A. K. W.; Woodbury, N. W. *J. Phys. Chem. B* **2002**, *106*, 12344.
- (68) Steffen, M.; Lao, K.; Boxer, S. *Science* **1995**, *264*, 810.
- (69) Chelli, R.; Ciabatti, S.; Cardini, G.; Righini, R.; Procacci, P. *J. Chem. Phys.* **1999**, *111*, 4218.
- (70) Goldstein, R. A.; Takiff, L.; Boxer, S. G. *Biochim. Biophys. Acta* **1988**, *934*, 253.
- (71) The calculation of the averaged dipole moment was carried out by performing 100-ps MD simulations of water and methanol in the NVE ensemble for systems containing 250 molecules. For methanol, we used the electrostatic force field described in ref 69.